Mathematics

https://www.aimspress.com/journal/Math

AIMS Mathematics, 11(2): 3193–3218.
DOI: 10.3934/math.2026128
Received: 20 November 2025
Revised: 13 January 2026
Accepted: 26 January 2026
Published: 02 February 2026

Research article

Bilinear feature-enhanced symbolic computation neural network method for solving the (1+1)-dimensional Caudrey–Dodd–Gibbon equation

Xia Li[1], **Jianglong Shen**[1,2,*], **Jingbin Liang**[1] **and Yu Gao**[1]

[1] Department of Mathematics and Physics, Yibin University, college street,Yibin, 644000, Sichuan, China

[2] Computational Physics Key Laboratory of Sichuan Province, Yibin University, college street,Yibin, 644000, Sichuan, China

* **Correspondence:** Email: jlshen@yibinu.edu.cn; +8617392950850; +8617392950850.

Abstract: The fifth-order dispersion nonlinear wave (1+1)-dimensional Caudrey–Dodd–Gibbon equation is a classic model describing soliton phenomena in fields such as plasma magnetosonic waves and optical fiber light pulses, and its exact solution is of great importance for revealing the laws of nonlinear wave motion. In this paper, an integrated framework combining bilinear polynomial feature enhancement, symbolic computation constraints, and neural network learning is proposed. Bilinear polynomial features such as x^2, t^2, and xt are introduced to break through the input limitation of original variables, broaden the boundary of the model in capturing nonlinear interactions between variables, and reduce errors caused by insufficient feature information. Symbolic computation is applied to the bilinear transformation derivation and conservation law analysis of the (1+1)-dimensional Caudrey–Dodd–Gibbon Equation to provide mathematical structure constraints for the neural network, and a collaborative mechanism of "symbolic reasoning guiding numerical learning" is constructed to improve the interpretability of the model. This framework breaks down the barriers between traditional numerical and pure neural network methods, realizes efficient and accurate solution of the (1+1)-dimensional Caudrey–Dodd–Gibbon equation, and provides a new path for the study of exact solutions of high-dimensional, variable-coefficient, and strongly nonlinear partial differential equations.

Keywords: (1+1)-dimensional Caudrey–Dodd–Gibbon equation; bilinearity; feature enhancement; symbolic computation; neural network
Mathematics Subject Classification: 35Q53, 65M60

1. Introduction

Nonlinear partial differential equations (NLPDEs) are core tools. They describe complex dynamic phenomena in fields such as fluid mechanics, plasma physics, and nonlinear optics. Their exact solutions are of great significance for revealing physical essence. In recent years, physics-informed neural networks (PINNs) have attracted much attention. This method uses the powerful approximation ability of neural networks. It can find approximate solutions of any NLPDEs. However, for complex NLPDEs, their accuracy is usually not satisfactory. The trial function method is a common symbolic computation method. It is used to find exact solutions of NLPDEs. Traditional solution methods (such as the Hirota bilinear method and the Bell polynomial method) can obtain some analytical solutions, but their adaptability to high-dimensional, variable-coefficient, and strongly nonlinear equations is limited. It is difficult to obtain exact analytical solutions for most. Traditional numerical methods (the finite difference method, the finite element method, etc.) rely on the discretization of the computational domain. In recent years, scholars have been continuously exploring state-of-the-art analytical and computational methods for solving nonlinear wave equations, and certain progress has been achieved [1–3]. With the integration of neural network and symbolic computation technology, bilinear neural network methods (BNNM) have emerged. These methods construct neural network models with bilinear operators. They integrate symbolic computation tools such as Mathematica and Maple. Thus, efficient solution to find exact solutions for complex NLPDEs. They show significant advantages over other methods, especially in the construction of solutions to (3+1)-dimensional equations and variable-coefficient equations.

Zhang et al. [4] first applied BNNM to the (2+1)-dimensional Caudrey–Dodd–Gibbon–Kotera–Sawada-like (CDGKSL) equation . They by constructing a “3-2-2” network model. Activation functions such as $\Phi_1(\xi_1) = \xi_1^2$, $\Phi_2(\xi_2) = \exp(\xi_2)$, were selected. Maple was used to collect coefficients and solve equations. Generalized and classical lump solutions were obtained, and zero-error was verified. This breakthrough overcame the limitation that traditional neural networks could only solve approximate solutions. Gai et al. [5] further expanded the network structure. Five types of multilayer models were designed for the (3+1)-dimensional generalized breaking soliton system. 4-2-2-1 and 4-2-3-1 models were also constructed. Multimorphological rogue wave solutions were obtained. To meet the solution needs of multivariable and variable-coefficient NLPDEs, Liu et al. [6] proposed a multivariable bilinear neural network method. Hidden layer neurons were defined as multivariable functions, such as $F_1(\xi_1, \xi_2) = \xi_1^2 + \xi_2^2$. Four types of models were constructed to solve the (2+1)-dimensional fourth-order nonlinear wave equation. Lump solutions, periodic wave solutions, and so forth, were obtained. Liu et al. [7] also proposed a variable-coefficient bilinear residual network method. Weights were set as time functions to adapt to variable coefficients $\beta_i(t)$. A new paradigm was provided for solving equations in inhomogeneous media. Symbolic computation is the core support of this method system. A Maple toolbox developed by Hao et al. realized the automation of bilinear equation coefficient collection, equation system solution, and solution verification [8]. The research on integrability and exact solutions of the Caudrey–Dodd–Gibbon (CDG) equation is a hot direction in the field of nonlinear science. Through Painlevé analysis and the Hirota bilinear method, scholars first verified the integrability of the CDG equation. This laid a foundation for the subsequent construction of exact solutions [9]. Kumar successfully constructed multisoliton solutions of the CDG equation based on the simplified Hirota technique. Through phase shift analysis, they found elastic collision characteristics between solitons. After collision, the wave form and amplitude remain unchanged [10]. The analytical method is employed to investigate approximate solutions of the fractional nonlinear CDG equation, enabling the acquisition of approximate solutions without linearization [11]. Deng et al. [12] investigated the 2+1-dimensional generalized CDGKS equation in fluid mechanics. By virtue of the Pfaffian technique and specific constraints imposed on the real constant g, they derived the nth-order Pfaffian solutions, from which the single-soliton and double-soliton solutions were further obtained. Some breather wave solutions and lump solutions of the CDG equation are obtained via the Hirota bilinear method with the assistance of the symbolic computation software Mathematica [13]. Khater et al. [14] derived the solutions to the CDG equation through the rigorous implementation of the Khater-II(KII) and variational iteration (VI) methodS. The research findings reveal new characteristics of the equation's behavior, providing deeper insights into nonlinear wave phenomena. Yokus conducted a comparative study on the $(G'/G, 1/G)$-expansion method and the $(1/G')$-expansion method for solving the CDG equation [15]. The modified simple equation method is a powerful and efficient approach, suitable for investigating the traveling wave solutions of nonlinear equations in the fields of applied mathematics, science, and engineering. Hossain et al. [16] applied the aforementioned method to study the CDG equation and obtained its exact solutions as well as those for traveling wave solutions. Ma et al. [17] studied the extended CDG equation. Soliton molecules of the extended CDG equation can be generated by utilizing the N-soliton solutions and a new velocity resonance condition. Sahinkaya obtained analytical results for the β-fractional CDG equation, which is utilized to solve complex problems in hydrodynamics, chemical kinetics, plasma physics, quantum field theory, crystal dislocations, and nonlinear optics via auxiliary methods [18]. Abdelhafeez proposed the Laplace residual power series method for solving the fractional CDG equation [19].

In interdisciplinary applications, Fathima D. emphasized that this model can elaborate on the propagation characteristics of magnetoacoustic waves, shallow water waves, and gravity-capillary waves in plasmas, and verified the influence of the fractional order on the physical behaviors of the solutions through simulations, thereby providing a theoretical basis for the physical applications of the solutions to the fractional CDG equation [20]. Ding et al. [21] utilized the equivalent moving frame method proposed by Olver, to obtain the differential invariants of the CDG equation and the coupled Korteweg–de Vries–modified Korteweg–de Vries (KdV–mKdV) equation, and further derived the algebra of differential invariants. Furthermore, the mathematical connection between the CDG equation and the Sawada–Kotera (SK) equation indicates that these models can uniformly describe nonlinear wave phenomena in plasma physics and fluid mechanics, thereby providing a theoretical bridge for interdisciplinary research [22]. In recent years, significant progress has been made in partial differential equation (PDE) solution methods based on neural networks. The PINNs method proposed by Raissi et al. integrates the PDE governing equation and boundary conditions into the loss function, to find meshless PDE solutions. It has been widely used in fields such as fluid mechanics and quantum mechanics [23]. Subsequently, Wang et al. [24] proposed the residual adaptive PirateNets architecture to stabilize deep PINN training, effectively resolving the poor derivative performance and unstable loss optimization issues observed in traditional deep networks during initialization. In terms of the integration of symbolic computation and neural networks, some studies have tried to use symbolic computation to generate initial parameters of neural networks. The convergence speed of the model was improved [25], but a unified framework combining feature enhancement and symbolic computation has not yet been formed. Breakthroughs in deep learning technology have provided a new mesh-independent path for PDE solutions. Among them, PINNs integrate PDE constraints into the loss function. The combination of data-driven and physical laws is realized [26–28]. However, most existing neural network methods directly use original spatial variable x and time variable t as input features, which are difficult to capture complex nonlinear interaction relationships between variables. As a result, the learning ability of the model for PDE solution structures is limited [29–31].

In summary, existing methods for solving the CDG equation and similar higher-order NLPDEs can be categorized into two main classes. Analytical methods [32–34] are capable of generating exact solutions but are strictly limited to integrable, low-dimensional, and constant-coefficient equations. Neural network-based methods [35–37] offer greater flexibility and are applicable to a wider range of PDEs. However, they typically use raw variables directly as inputs, which limits their ability to capture the complex nonlinear interactions inherent in higher-order NLPDEs such as the CDG equation, thereby restricting our understanding of many physical phenomena. Therefore, bridging these gaps is crucial for both theoretical and applied research.

The proposed bilinear feature-enhanced symbolic computation neural network (BFESCNN) method improves model interpretability and accuracy through a fusion framework of bilinear polynomial feature enhancement, symbolic computation constraints. and neural network learning. By introducing bilinear polynomial features x^2, t^2, xt as input enhancements, we break the limitations of original variable inputs, effectively capture nonlinear interactions between variables, and reduce errors caused by insufficient feature information. Simultaneously, symbolic computation is applied to processes such as bilinear transformation derivation and conservation law analysis, providing mathematical structural constraints for the neural network. This approach constructs a collaborative mechanism of symbolic reasoning to guide numerical learning, fundamentally alleviating the ‘black-box’ problem of traditional neural networks. Furthermore, a synergistic mechanism which integrates analytical and numerical methods is established which clearly distinguishes between analytical deduction steps (manual mathematical reasoning) and symbolic execution steps (automated computation via Maple/Mathematica). This approach not only preserves the mathematical rigor of analytical methods but also leverages the efficient solving capability of neural networks, achieving a balance between solution accuracy and computational efficiency. In this study, a BFESCNN model suitable for the fifth-order dispersive nonlinear wave (1+1)-dimensional CDG equation [38–40]

$$u_t + u_{xxxxx} + 30u_{xxx} + 30u_x u_{xx} + 180u_x^2 u_{xx} = 0 \tag{1.1}$$

is constructed. Through the polynomial feature enhancement strategy, the learning ability of the neural network for nonlinear relationships between variables is improved. Efficient prediction of the exact solution of the equation is realized, and the symbolic computation module is integrated. Automatic analysis of the mathematical structure of the (1+1)-dimensional CDG equation and constraint embedding are included. The interpretability and generalization ability of the model are enhanced. A general framework is provided for solving other nonlinear PDEs. The advantages of the BFESCNN method in solution accuracy, stability, and computational efficiency are verified through numerical experiments. Its application potential in fields such as plasma physics and optical fiber communication is also explored.

2. BFESCNN framework

The BFESCNN model is shown in Figure 1. First, the bilinear form of the original equation was obtained through bilinear transformation. Then, the expression of the bilinear function f was constructed using the feature-enhanced symbolic computation neural network model. Next, the expression f was substituted into the bilinear equation. A complex algebraic polynomial was obtained. By collecting the coefficients of x, y, ..., an algebraic equation system regarding weights w and b was obtained. Finally, the algebraic equation system was solved. The coefficient solutions were obtained and substituted into its bilinear transformation u. The exact analytical solution of the nonlinear partial differential equation was thus obtained.

To convert the (1+1)-dimensional CDG equation into its bilinear form via the Hirota bilinear transformation, let

$$u(x,t) = 2(\ln f)_{xx}, \tag{2.1}$$

where $f = f(x,t)$ denotes the transformation function, implying $(\ln f)_{xx} = \frac{u}{2}$. We utilize the Hirota bilinear operator defined as

$$D_t^m D_x^n f \cdot g = \sum_{k=0}^{m} \sum_{l=0}^{n} (-1)^k \binom{m}{k} \binom{n}{l} \frac{\partial^{m-k}}{\partial t^{m-k}} \frac{\partial^{n-l}}{\partial x^{n-l}} f \cdot \frac{\partial^k}{\partial t^k} \frac{\partial^l}{\partial x^l} g$$

to reorganize the equation term by term. For the space-time mixed term u_t, it corresponds to the bilinear operator $D_t D_x$. When $g = f$, this operator expands as $D_t D_x f \cdot f = f_t f_x - f_x f_t$; for the sixth-order spatial term u_{xxxxxx}, it is associated with the bilinear operator D_x^6, which expands to $f_{xxxxxx} f - 6 f_{xxxxx} f_x + 15 f_{xxxx} f_{xx} - 10 f_{xxx}^2$.

Consequently, the Hirota bilinear form of the fifth-order dispersive nonlinear (1+1)-dimensional CDG equation is given by

$$\left(D_t D_x + D_x^6\right) f \cdot f = 0,$$

which explicitly expands to

$$f_t f_x - f_x f_t + f_{xxxxxx} f - 6 f_{xxxxx} f_x + 15 f_{xxxx} f_{xx} - 10 f_{xxx}^2 = 0. \tag{2.2}$$

The tensor network model is shown in Figure 1.

$$f = \omega_{l_n,j} \Phi_{l_n}(\xi_{l_n}), \quad \xi_{l_i} = \omega_{l_{i-1},j} \Phi_{l_{i-1}}(\xi_{l_{i-1}}) + b_i,\ i = 1, 2, \cdots, n; \tag{2.3}$$

in $\omega_{i,j}$, the weight coefficient of neurons from i to j was denoted as ω. Φ was the activation function. If the last hidden layer satisfied the condition $\Phi_{l_n}(\xi) \geq 0$, the model could be extended to any function. $l_n = \{m_{n-1} + 1, m_{n-1} + 2, \ldots, n\}$ represented the nth layer space of the feature-enhanced symbolic computation neural network in Figure 1. $l_0 = \{x_1, x_2, \ldots, x_n\}$, $l_1 = \{1, 2, \ldots, m_1\}$, $l_i = \{m_{i-1} + 1, m_{i-1} + 2, \ldots, m_i\}$ $(i = 2, 3, \ldots, n-1)$, and j was a constant. The main steps of the feature-enhanced symbolic computation neural network model were as follows:

Step 1. The bilinear Eq (2.2) is derived by substituting the bilinear transformation Eq (2.1) into Eq (1.1).

Step 2. Construct polynomial features based on variables and obtain Eq (2.3), then substitute Eq (2.3) into the bilinear Eq (2.2) to obtain a new set of equations.

Step 3. Gather the coefficients of each term in the system of equations obtained in the second step, for instance,

$$x_i, x_i^2, x_i^3, \dots, (i = 1, 2, \dots, n), F'(\xi), F''(\xi), \dots, \tag{2.4}$$

set all the collected coefficients to zero, and a system of nonlinear algebraic equations is obtained.

Step 4. Solve the system of nonlinear algebraic equations obtained in the third step using Maple (or Mathematica) software to get the coefficient solutions for "b" and "ω".

Step 5. Substitute the solution obtained in the fourth step into the following linear transformation equation:

$$u = 2[\ln \omega_{l_i,j}\Phi_{l_i}(\xi_{l_i})]_{xx}, \quad \xi_{l_i} = \omega_{l_{i-1},l_i}\Phi_{l_{i-1}}(\xi_{l_{i-1}}) + b_i, \; i = 1, 2, \dots, n. \tag{2.5}$$

From the above steps, the exact analytical solutions of the nonlinear partial differential Eq (1.1) can be obtained.

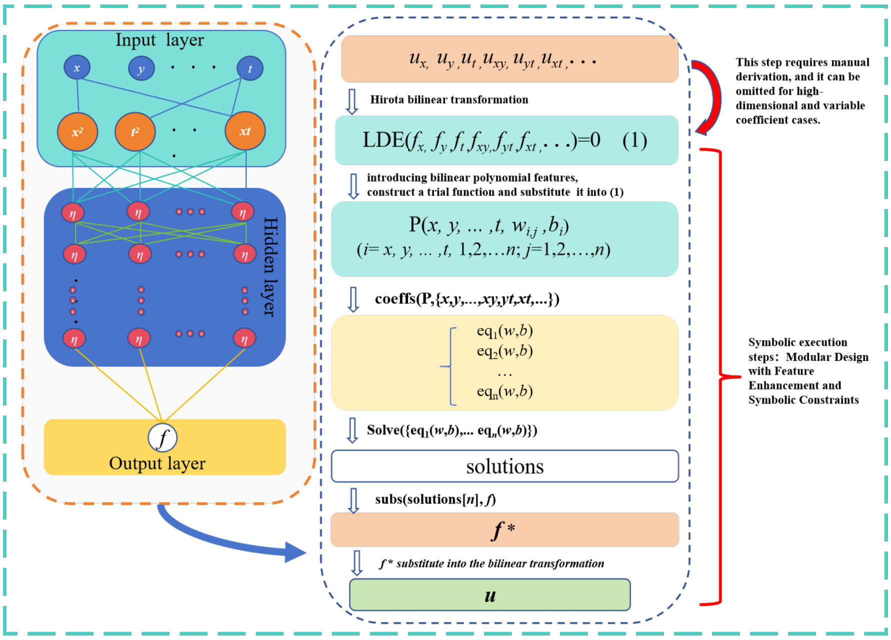

Figure 1. BFESCNN model.

The advantages of the bilinear feature-enhanced symbolic computation neural network are as follows:

1. It breaks through the limitation of traditional original variable input;
2. it expands the model's boundary for capturing nonlinear relationships;
3. it reduces solution errors caused by insufficient feature information;
4. it enables the construction of exact analytical solutions for nonlinear partial differential equations.

Comparison with traditional neural network methods or symbolic methods is shown in Tables 1 and 2.

Table 1. Core differences between BFESCNN and classical related methods.

Comparison dimension	**BFESCNN**	**BNNM**	**Hirota bilinear method**	**Jacobi elliptic function expansion method**
Core objective and output result	Aims to obtain exact analytical solutions; outputs explicit mathematical expressions (e.g., soliton solutions) with interpretable physical meanings	Focuses on improving numerical fitting accuracy; only outputs discrete numerical results without explicit expressions	Derives multitype exact solutions (solitons, breathers, lumps) for integrable PDEs; outputs explicit symbolic analytical expressions	Constructs periodic/quasiperiodic wave solutions; outputs explicit expressions based on Jacobi elliptic functions (sn, cn, dn)
Core idea	Bilinear transformation with feature-enhanced symbolic computation and neural network (e.g., x^2, t^2,xt)	Bilinear transformation with symbolic computation and neural network	Transform PDEs into bilinear forms via substitution; solve with Hirota D-operator ($D_x^m D_t^n f \cdot f = 0$)	Expands solutions as elliptic function series; determines coefficients by nonlinear dispersion balance
Advantages	vs BNNM: Breaks original variables' input limit, broadens capturing nonlinear interactions, reduces feature info shortage errors	Exactness of analytical solutions, mathematical rigor	Direct solving method, no complex transform, applicable to high-dimensional integrable PDEs	Captures periodic wave behaviors, applicable to non-integrable PDEs with periodic solutions
Function and position of neural network	Learns the mapping of "enhanced features toward analytical solutions"; compact structure, output analytical solution forms	Performs nonlinear numerical fitting; relies on large-scale labeled data, only output discrete values	No neural network; pure analytical symbolic derivation	No neural network; pure analytical function expansion
Data dependence	Low; no need for massive training samples, only a small number of parameter samples to verify mapping validity	High; requires large-scale labeled data for fitting	None; pure analytical method with no data required	None; pure analytical method with no data required

Table 2. Core differences between BFESCNN and PINN series methods.

Comparison dimension	**PINN (Original)**	**Ψ-NN**	**Mixed-training PINNs**
Core objective and output result	Aims to reduce numerical training errors; outputs approximate numerical solutions with physical constraints (non-analytical form)	Balances analytical interpretability and numerical accuracy; outputs semianalytical solutions (symbolic framework and numerical correction)	Enhances generalization via mixed data; outputs improved approximate numerical solutions with better adaptability
Core idea	PDE constraints and neural network	Symbolic basis (bilinear terms) and neural network residual correction	Supervised and unsupervised learning, PDE regularization mitigates data scarcity
Advantages	Data-efficient, physically interpretable, mesh-free	Retains analytical interpretability; handles mild non-integrability	Reduces reliance on labeled data; better sparse data performance
Function and position of neural network	Optimizes numerical solutions; depends on data iteration; requires interpolation for physical interpretation	Learns residual errors for semianalytical correction; neural network as a "corrector"	Optimizes dual loss function; neural network as a regularized fitter
Data dependence	High; requires sufficient data for iterative optimization; data volume directly affects accuracy	Low; symbolic basis reduces data demand with small datasets	Moderate; mixed data (labeled and unlabeled) reduces reliance on labeled samples

This method, as a model, contained only one hidden layer. To illustrate, in a single-hidden-layer feature-enhanced network, two specific functions were given. This single-hidden-layer feature-enhanced network could cover the test functions constructed by the bilinear method, as shown in Figure 2. Alternatively, in a double-hidden-layer feature-enhanced network, four specific functions were given. This double-hidden-layer feature-enhanced network could cover the test functions constructed by the bilinear method, as shown in Figure 3.

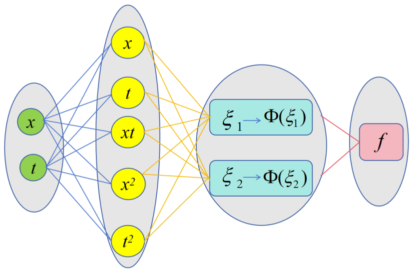

Figure 2. Single-hidden-layer feature-enhanced 2-5-2-1 neural network model.

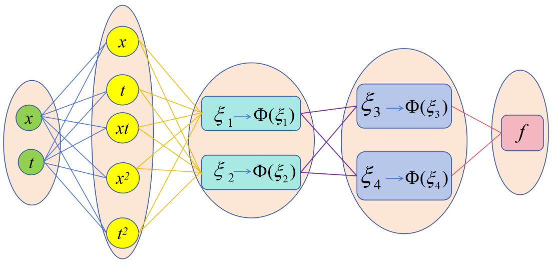

Figure 3. Double-hidden-layer feature-enhanced 2-5-2-2-1 neural network model.

3. Exact solution of the (1+1)-dimensional CDG equation solved by the BFESCNN method

The BFESCNN algorithm was applied. Specifically, the single-hidden-layer feature-enhanced 2-5-2-1 neural network model and the double-hidden-layer feature-enhanced 2-5-2-2-1 neural network model were used. Corresponding trial functions were selected respective to each case. The exact solutions of the (1+1)-dimensional CDG equation were obtained. 3D graphs, density graphs, curve graphs, and contour graphs of the solutions were plotted. The characteristics of the solutions were analyzed.

3.1. Single-hidden-layer feature-enhanced 2-5-2-1 neural network model

3.1.1. Model 2-5-2-1 Case 1

The mathematical expression corresponding to the single-hidden-layer feature-enhanced 2-5-2-1 neural network model in Figure 4 was selected as the test function.

$$\begin{aligned} \xi_1 &= w_{x,1}\cdot x + w_{t,1}\cdot t + w_{xt,1}\cdot xt + w_{x^2,1}\cdot x^2 + w_{t^2,1}\cdot t^2 + b_1,\\ \xi_2 &= w_{x,2}\cdot x + w_{t,2}\cdot t + w_{xt,2}\cdot xt + w_{x^2,2}\cdot x^2 + w_{t^2,2}\cdot t^2 + b_2,\\ f &= w_{1,f}\cdot \xi_1^2 + w_{2,f}\cdot \xi_2^2 + b_3. \end{aligned} \tag{3.1}$$

As shown in Figure 4, the activation functions $\Phi_1(\xi_1) = \xi_1^2$, $\Phi_2(\xi_2) = \xi_2^2$ were set. Thus, the test functions for the solution were obtained as follows:

$$\begin{aligned} f = {} & w_{1,f}\cdot\left(w_{x,1}\cdot x + w_{t,1}\cdot t + w_{xt,1}\cdot xt + w_{x^2,1}\cdot x^2 + w_{t^2,1}\cdot t^2 + b_1\right)^2\\ & + w_{2,f}\cdot\left(w_{x,2}\cdot x + w_{t,2}\cdot t + w_{xt,2}\cdot xt + w_{x^2,2}\cdot x^2 + w_{t^2,2}\cdot t^2 + b_2\right)^2 + b_3; \end{aligned} \tag{3.2}$$

among them, $b_i\,(i=1,2,3)$, $w_{j,f}\,(j=1,2)$, and $w_{k,1}\,(k=x,t,xt,x^2,t^2)$ were real numbers.

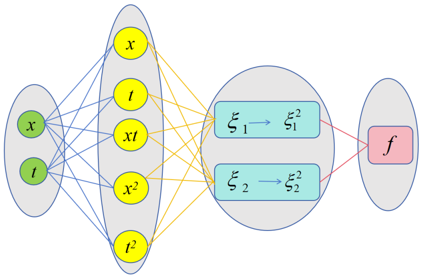

Figure 4. 2-5-2-1 neural network model with given activation functions $\Phi_1(\xi_1) = \xi_1^2$, $\Phi_2(\xi_2) = \xi_2^2$.

The solution test function (3.2) was substituted into the bilinear Eq (2.2). A complex algebraic equation was obtained. The coefficients of each term were collected and set to 0. Then, the equation could be satisfied. At this point, a system of algebraic equations was obtained and solved, yielding the following results:

$$\begin{aligned} w_{t,4} &= -\frac{w_{t,2}\, w_{x^2,2}^2}{w_{x^2,1}^2},\; w_{t,1} = -\frac{w_{x^2,1}\, w_{t,2}}{w_{x^2,2}}, \\ w_{xt,1} &= \frac{w_{xt,2}\, w_{x^2,1}}{w_{x^2,2}},\; w_{t^2,1} = -\frac{w_{t^2,2}\, w_{x^2,1}^2}{w_{x^2,2}^2}, \\ b_4 &= 0,\; w_{xt,2} = 0,\; w_{xt,1} = 0. \end{aligned} \tag{3.3}$$

Substitute (3.3) into the test function (3.2). Then, through the bilinear transformation (2.1), the explicit solution of the (1+1)-dimensional CDG Eq (1.1) was obtained as follows:

$$\begin{aligned} u = &\frac{8w_{x^2,1}w_{x^2,2}}{(2x^2 w_{x^2,1}w_{x^2,2} + 2xw_{x^2,2}w_{x^2,1} + b_1 w_{x^2,2} + b_2 w_{x^2,1})} \\ &- \frac{2\left(4xw_{x^2,1}w_{x^2,2} + 2w_{x^2,2}w_{x^2,1}\right)^2}{(2x^2 w_{x^2,1}w_{x^2,2} + 2xw_{x^2,2}w_{x^2,1} + b_1 w_{x^2,2} + b_2 w_{x^2,1})^2}. \end{aligned} \tag{3.4}$$

To verify the accuracy of Result (3.4), the analytical solution (3.4) was substituted into the left-hand side (LHS) of Eq (1.1). With the aid of Maple software, the simplified result demonstrated that the LHS of Eq (1.1) equals zero. This indicates that the analytical solution (3.4) is reliable, accurate, and error-free. It also illustrates the advantage of this method: In comparison with classical neural network methods, which only yield approximate solutions, the bilinear feature-enhanced symbolic computation neural network algorithm enables the acquisition of exact analytical solutions. In solution (3.4), $w_{x^2,2} = 1, w_{x^2,1} = 2, b_1 = 1, w_{x,2} = 1, b_2 = 1$ were set. The graph of the solution could then be plotted (Figure 5).

Figure 5(a) displays the 3D graph when $t \in (-30, 30)$ and $x \in (-30, 30)$. The "pleat depth" and "asymmetric morphology" of the surface embody the nonlinear interaction in the (1+1)-dimensional CDG equation, and the amplitude of the wave is nonuniformly distributed in space. The difference between the low-value regions (deep pleats) and high-value regions (shallow pleats) reflects the localization of energy.

Figure 5(b) is the contour graph of solution (3.4). The high-value regions (red-brown) and low-value regions (blue-purple) are distributed in stripes along the x-axis, indicating that the amplitude of the wave is periodically stratified in space. The contour lines (blue vertical lines) are arranged in parallel and show no obvious bending or divergence as time t elapses, verifying that the wave propagates in a fixed direction with a stable shape, which is consistent with the propagation trend in the 3D graph.

Figure 5(c) is a density graph. A continuous color gradient (color bar on the right) is used to show the distribution of u in the x-t plane, where purple represents low-value regions (sparse energy), and colored stripes represent high-value regions (concentrated energy). The strong contrast between high-brightness regions (red-yellow) and low-brightness regions (purple) in the stripes reflects the energy concentration characteristic of the solution to the (1+1)-dimensional CDG equation, and energy is mainly distributed in the colored stripes with extremely low energy in the background field.

Figure 5(d) is a curve graph of u versus x in the domain $t \in (-60, 60)$. The horizontal axis is x, the vertical axis is u, and multiple colored curves correspond to the distribution of $u(x)$ at different times t. The peak positions of curves at different t shift along the x-axis, which is consistent with the propagation direction in the 3D graph and the contour graph. Moreover, the depth and width of the peaks are basically stable, verifying the time invariance of the solution.

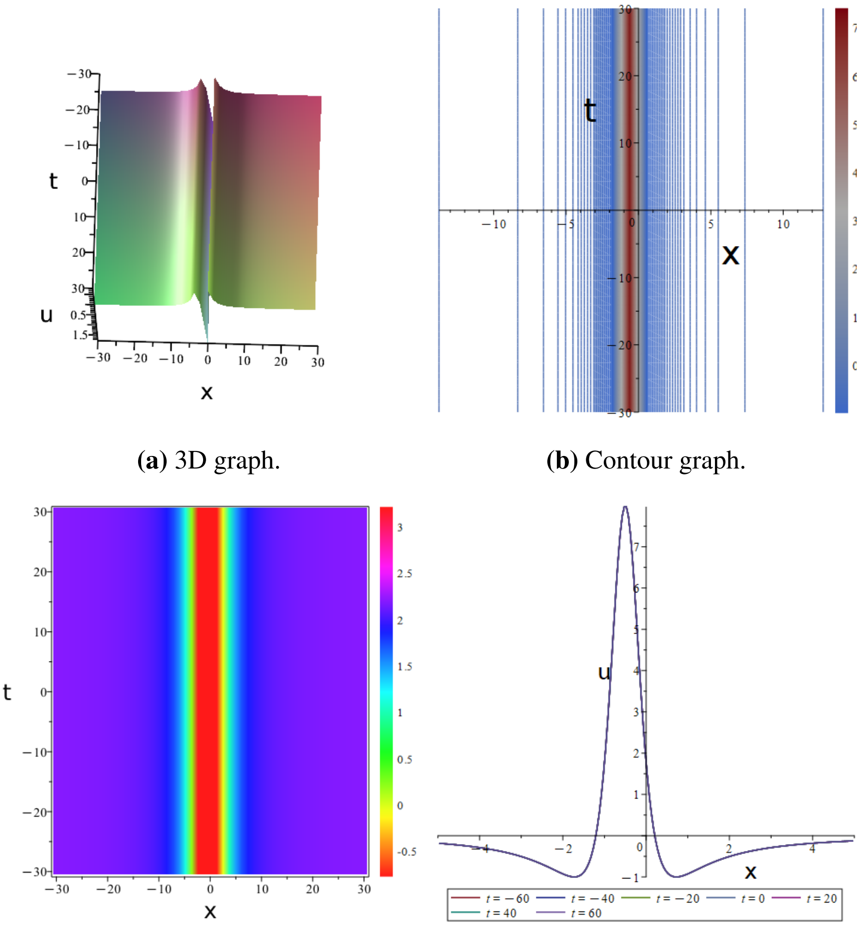

(a) 3D graph.

(b) Contour graph.

(c) Density graph.

(d) Curve graph.

Figure 5. 3D graph, contour graph, density graph, and curve graph of the solution to Eq (3.4).

3.1.2. Model 2-5-2-1 Case 2

Similar to Model 2-5-2-1 Case 1, The mathematical expression corresponding to the single-hidden-layer feature-enhanced 2-5-2-1 neural network model in Figure 6 was selected as the test function.

$$\begin{aligned} \xi_1 &= w_{x,1} \cdot x + w_{t,1} \cdot t + w_{xt,1} \cdot xt + w_{x^2,1} \cdot x^2 + w_{t^2,1} \cdot t^2 + b_1, \\ \xi_2 &= w_{x,2} \cdot x + w_{t,2} \cdot t + w_{xt,2} \cdot xt + w_{x^2,2} \cdot x^2 + w_{t^2,2} \cdot t^2 + b_2, \\ f &= w_{1,f} \cdot \operatorname{sech}(\xi_1) + w_{1,f} \cdot \xi_2^2 + b_3. \end{aligned} \tag{3.5}$$

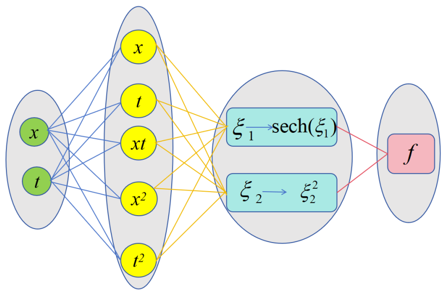

Figure 6. 2-5-2-1 neural network model with given activation functions $\Phi_1(\xi_1) = \operatorname{sech}(\xi_1)$, $\Phi_2(\xi_2) = \xi_2^2$.

As shown in Figure 6, the activation functions $\Phi_1(\xi_1) = \operatorname{sech}(\xi_1)$, $\Phi_2(\xi_2) = \xi_2^2$ were set. Thus, the test functions for the solution were obtained as follows:

$$\begin{aligned} f = {} & w_{1,f} \cdot \operatorname{sech}\left(w_{x,1} \cdot x + w_{t,1} \cdot t + w_{xt,1} \cdot xt + w_{x^2,1} \cdot x^2 + w_{t^2,1} \cdot t^2 + b_1\right) \\ & + w_{2,f} \cdot \left(w_{x,2} \cdot x + w_{t,2} \cdot t + w_{xt,2} \cdot xt + w_{x^2,2} \cdot x^2 + w_{t^2,2} \cdot t^2 + b_2\right)^2 + b_3; \end{aligned} \tag{3.6}$$

among them, $b_i\,(i = 1, 2, 3)$, $w_{j,f}\,(j = 1, 2)$ and $w_{k,1}\,(k = x, t, xt, x^2, t^2)$ were real numbers.

The solution test function (3.6) was substituted into the bilinear Eq (2.2). A complex algebraic equation was obtained. The coefficients of each term were collected and set to 0. Then the equation could be satisfied. At this point, a system of algebraic equations was obtained and solved, yielding the following results:

$$w_{t^2,1} = -\frac{w_{t,1}}{2t}, w_{t^2,2} = -\frac{w_{t,2}}{2t}, w_{x,1} = 0, w_{xt,1} = 0, w_{x,2} = 0, w_{x^2,1} = 0, w_{x^2,2} = 0. \tag{3.7}$$

Substitute (3.7) into the test function (3.6). Then, through the bilinear transformation (2.1), the explicit solution of the (1+1)-dimensional CDG Eq (1.1) was obtained as follows:

$$\begin{aligned} u = {} & \frac{4 w_{2,f} w_{x^2,2}^2}{b_3 + w_{1,f} \operatorname{sech}\left(\frac{w_{t,1}}{2} + b_1\right) + \frac{w_{2,f}\left(w_{t,2} + 2x w_{x,2} + 2b_2\right)^2}{4}} \\ & - \frac{2 w_{2,f}^2 \left(w_{t,2} + 2x w_{x,2} + 2b_2\right)^2 w_{x^2,2}^2}{\left(b_3 + w_{1,f} \operatorname{sech}\left(\frac{w_{t,1}}{2} + b_1\right) + \frac{w_{2,f}\left(w_{t,2} + 2x w_{x,2} + 2b_2\right)^2}{4}\right)^2}. \end{aligned} \tag{3.8}$$

To verify the accuracy of Result (3.8), the analytical solution (3.8) was substituted into the LHS of Eq (1.1). With the aid of Maple software, the simplified result demonstrated that the LHS of Eq (1.1) equals zero. This indicates that the analytical solution (3.8) is reliable, accurate, and error-free. It also underscores the advantage of the proposed method: In contrast to classical neural network methods, which only yield approximate solutions, the bilinear feature-enhanced symbolic computation neural network algorithm enables the acquisition of exact analytical solutions. In solution (3.8), $w_{2,f} = 1, w_{t,1} = 1, b_3 = 1, b_1 = 1, w_{t,2} = 1, w_{x,2} = 1, b_2 = 1, w_{1,f} = 1$ were set. The graph of the solution could then be plotted (Figure 7).

Figure 7(a) displays the 3D graph when $t \in (-30, 30)$ and $x \in (-30, 30)$. The "fold depth" of the graph corresponds to the difference in wave amplitudes, where deep-fold regions represent high-amplitude wave crests/troughs, and shallow-fold regions represent low-amplitude background fields, embodying the nonlinear wave characteristics of the (1+1)-dimensional CDG equation solution with multiscale and nonuniform distribution.

Figure 7(b) is the contour graph of solution (3.8). A color gradient (color bar on the right) is used to reflect the magnitude of u, and contour lines (blue lines) connect points with equal u. The contour lines are arranged in an oblique parallel manner, indicating that the wave propagates along a fixed direction, which is consistent with the propagation trend of the 3D graph. Moreover, the spatial morphology of the wave is stable during propagation, and the spacing and density of contour lines verify the propagation stability of the solution.

Figure 7(c) is a density graph. A continuous color gradient (color bar on the right) is used to show the distribution of u in the x-t plane, where high-value regions (red-yellow) are energy-concentrated areas, and low-value regions (blue-purple) are energy-sparse areas. The dark "point arrays" embedded in the color stripes are the core energy bodies of the wave, embodying the localization characteristic of the (1+1)-dimensional CDG equation solution, where energy is concentrated in a limited space, and the energy of the background field is extremely low.

Figure 7(d) is a curve graph of u versus x in the domain $(-150, 150)$. The horizontal axis is x, the vertical axis is u, and multiple colored curves correspond to the distribution of $u(x)$ at different times t. Each curve exhibits a periodic multipeak morphology. The number and spacing of peaks correspond to the multisoliton and multiwave interference characteristics of the (1+1)-dimensional CDG equation solution. The peak height reflects the wave amplitude, the peak width reflects the spatial scale of the wave, and the peak spacing reflects the interaction period of the waves.

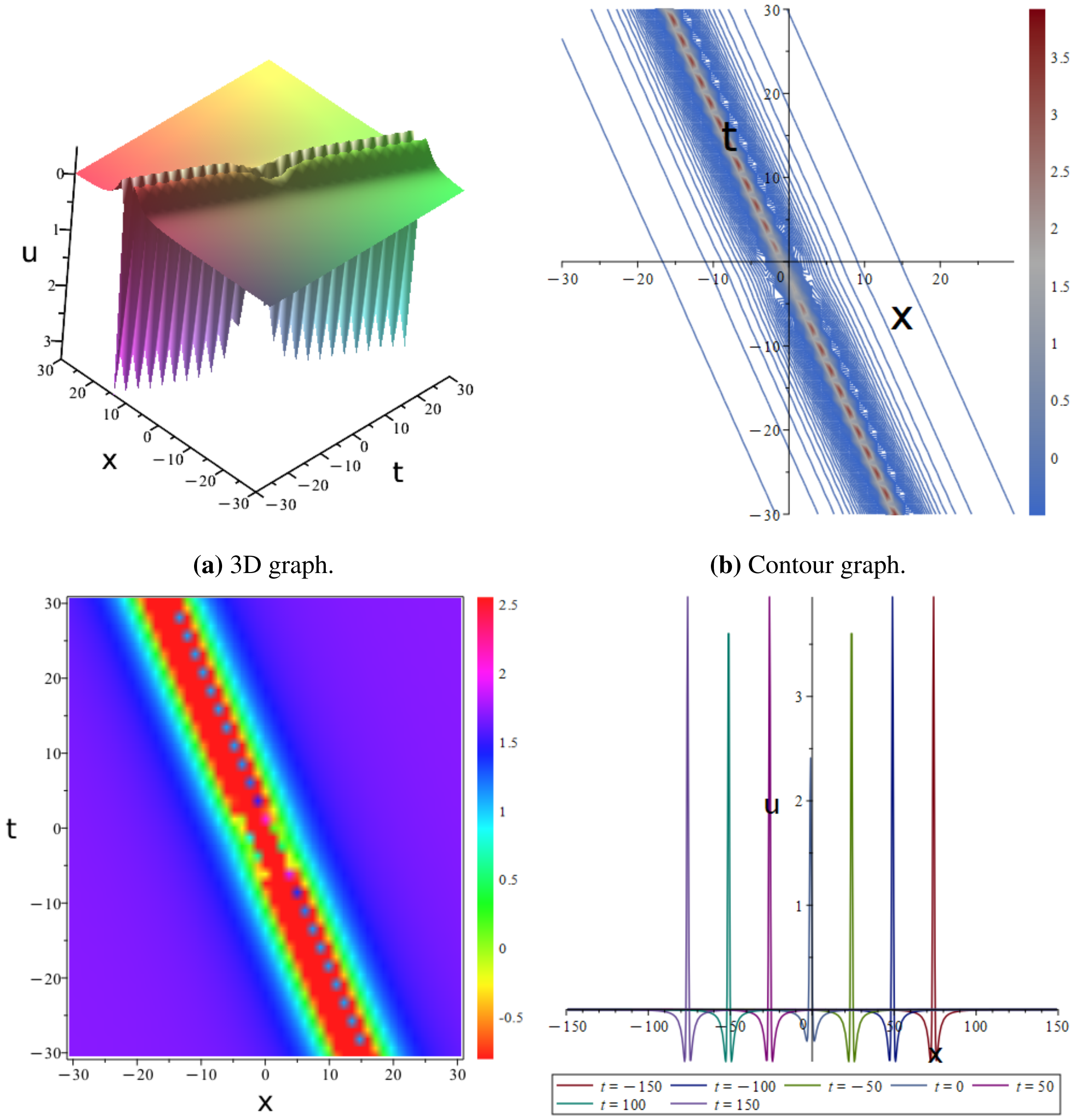

(**a**) 3D graph. (**b**) Contour graph.

(**c**) Density graph. (**d**) Curve graph.

Figure 7. 3D graph, contour graph, density graph, and curve graph of the solution to Eq (3.8).

3.2. Double-hidden-layer feature-enhanced 2-5-2-2-1 neural network model

3.2.1. Model 2-5-2-2-1 Case 1

The mathematical expression corresponding to the double-hidden-layer feature-enhanced 2-5-2-2-1 neural network model in Figure 8 was selected as the test function.

$$\begin{aligned} \xi_1 &= w_{x,1} \cdot x + w_{t,1} \cdot t + w_{xt,1} \cdot xt + w_{x^2,1} \cdot x^2 + w_{t^2,1} \cdot t^2 + b_1, \\ \xi_2 &= w_{x,2} \cdot x + w_{t,2} \cdot t + w_{xt,2} \cdot xt + w_{x^2,2} \cdot x^2 + w_{t^2,2} \cdot t^2 + b_2, \\ \xi_3 &= w_{1,3} \cdot \xi_1 + w_{2,3} \cdot \xi_2 + b_3, \\ \xi_4 &= w_{1,3} \cdot \xi_1 + w_{2,3} \cdot \xi_2 + b_4, \\ f &= w_{3,f} \cdot \xi_3^2 + w_{4,f} \cdot \xi_4^2 + b_5. \end{aligned} \tag{3.9}$$

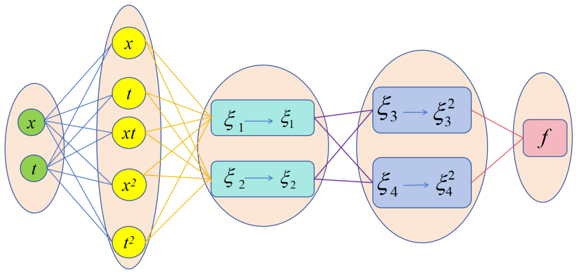

Figure 8. 2-5-2-2-1 neural network model with given activation functions $\Phi_1(\xi_1) = \xi_1$, $\Phi_2(\xi_2) = \xi_2$, $\Phi_3(\xi_3) = \xi_3^2$, $\Phi_4(\xi_4) = \xi_4^2$.

As shown in Figure 8, the activation functions $\Phi_1(\xi_1) = \xi_1$, $\Phi_2(\xi_2) = \xi_2$, $\Phi_3(\xi_3) = \xi_3^2$, $\Phi_4(\xi_4) = \xi_4^2$ were set. Thus, the test functions for the solution were obtained as follows:

$$\begin{aligned} f = b_5 &+ w_{3,f}\Big(w_{1,3}\left(t^2 w_{t^2,1} + txw_{xt,1} + x^2 w_{x^2,1} + tw_{t,1} + xw_{x,1} + b_1\right) \\ &+ w_{2,3}\left(t^2 w_{t^2,2} + txw_{xt,2} + x^2 w_{x^2,2} + tw_{t,2} + xw_{x,2} + b_2\right) + b_3\Big)^2 \\ &+ w_{4,f}\Big(w_{1,3}\left(t^2 w_{t^2,1} + txw_{xt,1} + x^2 w_{x^2,1} + tw_{t,1} + xw_{x,1} + b_1\right) \\ &+ w_{2,3}\left(t^2 w_{t^2,2} + txw_{xt,2} + x^2 w_{x^2,2} + tw_{t,2} + xw_{x,2} + b_2\right) + b_3\Big)^2; \end{aligned} \tag{3.10}$$

among them, $b_i\,(i = 1, 2, 3)$, $w_{j,f}\,(j = 1, 2)$ and $w_{k,1}\,(k = x, t, xt, x^2, t^2)$ were real numbers.

The solution test function (3.10) was substituted into the bilinear Eq (2.2). A complex algebraic equation was obtained. The coefficients of each term were collected and set to 0. Then, the equation could be satisfied. At this point, a system of algebraic equations was obtained and solved, yielding the following results:

$$\begin{aligned} w_{t,1} &= -\frac{w_{2,3} w_{t,2}}{w_{1,3}}, \quad w_{x,1} = -\frac{w_{x,2} w_{2,3}}{w_{1,3}}, \\ w_{t^2,1} &= \frac{w_{t^2,2} w_{2,3}}{w_{1,3}}, \quad w_{x^2,1} = -\frac{w_{x^2,2} w_{2,3}}{w_{1,3}}. \end{aligned} \tag{3.11}$$

Substitute (3.11) into the test function (3.10). Then, through the bilinear transformation (2.1), the explicit solution of the (1+1)-dimensional CDG Eq (1.1) was obtained as follows:

$$\begin{cases} u = \frac{2(2B^2 w_{3,f} + 2B^2 w_{4,f})}{A^2 w_{3,f} + A^2 w_{4,f} + b_3} - \frac{-2(2A w_{3,f} B)}{\left(A^2 w_{3,f} + (A^2 w_{4,f} + b_3)\right)^2} + \frac{2(A w_{4,f} B)^2}{\left(A^2 w_{3,f} + (A^2 w_{4,f} + b_3)\right)^2}, \\ A = (x w_{x,2} + b_2) w_{2,3} + (x w_{x,1} + b_1) w_{1,3} + b_3, \\ B = w_{1,3} w_{x,1} + w_{2,3} w_{x,2}. \end{cases} \tag{3.12}$$

To verify the accuracy of Result (3.12), the analytical solution (3.12) was substituted into the LHS of Eq (1.1). With the aid of Maple software, the simplified result showed that the LHS of Eq (1.1) equaled zero. This confirmed that the analytical solution (3.12) is reliable, accurate, and error-free. It further highlights the advantage of the present method: In comparison with classical neural network methods, which merely yield approximate solutions, the bilinear feature-enhanced symbolic computation neural network algorithm enables the acquisition of exact analytical solutions. In solution (3.12), $w_{3,f} = 1, b_3 = 1, b_1 = 1, w_{x,2} = 1, b_2 = 1, w_{4,f} = 1, w_{t,1} = 2, w_{1,3} = 1, w_{2,3} = 1, b_5 = 1$ were set. The graph of the solution could then be plotted (Figure 9).

Figure 9(a) displays the 3D graph when $t \in (-150, 150)$ and $x \in (-150, 150)$. It presents a double "slope" structure, and the color gradient (blue-purple transition) on the left and right sides corresponds to the amplitude distribution of u. The middle "concave" region is the low-value region of u, whereas the two sides are high-value regions. The "asymmetric concavity" of the surface embodies the nonlinear interaction of the (1+1)-dimensional CDG equation, and the difference between the low-value region (concavity) and the high-value region (slope) reflects the localized concentration of energy.

Figure 9(b) is the contour graph of solution (3.12). A color gradient (color bar on the right) is used to map the magnitude of u (red-yellow for high values, blue-purple for low values), and the red vertical lines are contour lines. The high-value regions (red-brown) and low-value regions (blue-purple) are distributed in bands along the x-axis, indicating that the amplitude of the wave is periodically stratified in space.

Figure 9(c) is a density graph. A continuous color gradient (color bar on the right) is used to show the distribution of u in the x-t plane, where red represents high-value regions (energy concentration) and colored stripes represent low-value regions (energy sparsity). Narrow colored stripes (green-blue-purple) are embedded in the red background, corresponding to the low-value regions of u, embodying the energy concentration characteristic of the (1+1)-dimensional CDG equation solution. Energy is mainly distributed in the red high-value regions, and energy-sparse bands only appear in local regions.

Figure 9(d) is a curve graph of u versus x in the domain $(-150, 150)$. The horizontal axis is x, the vertical axis is u, and multiple colored curves correspond to the distribution of $u(x)$ at different times t. The peak positions of curves at different t shift along the x-axis, which is consistent with the propagation directions of the 3D graph and the contour graph. Moreover, the depth and width of the peaks are basically stable, verifying the time invariance of the solution.

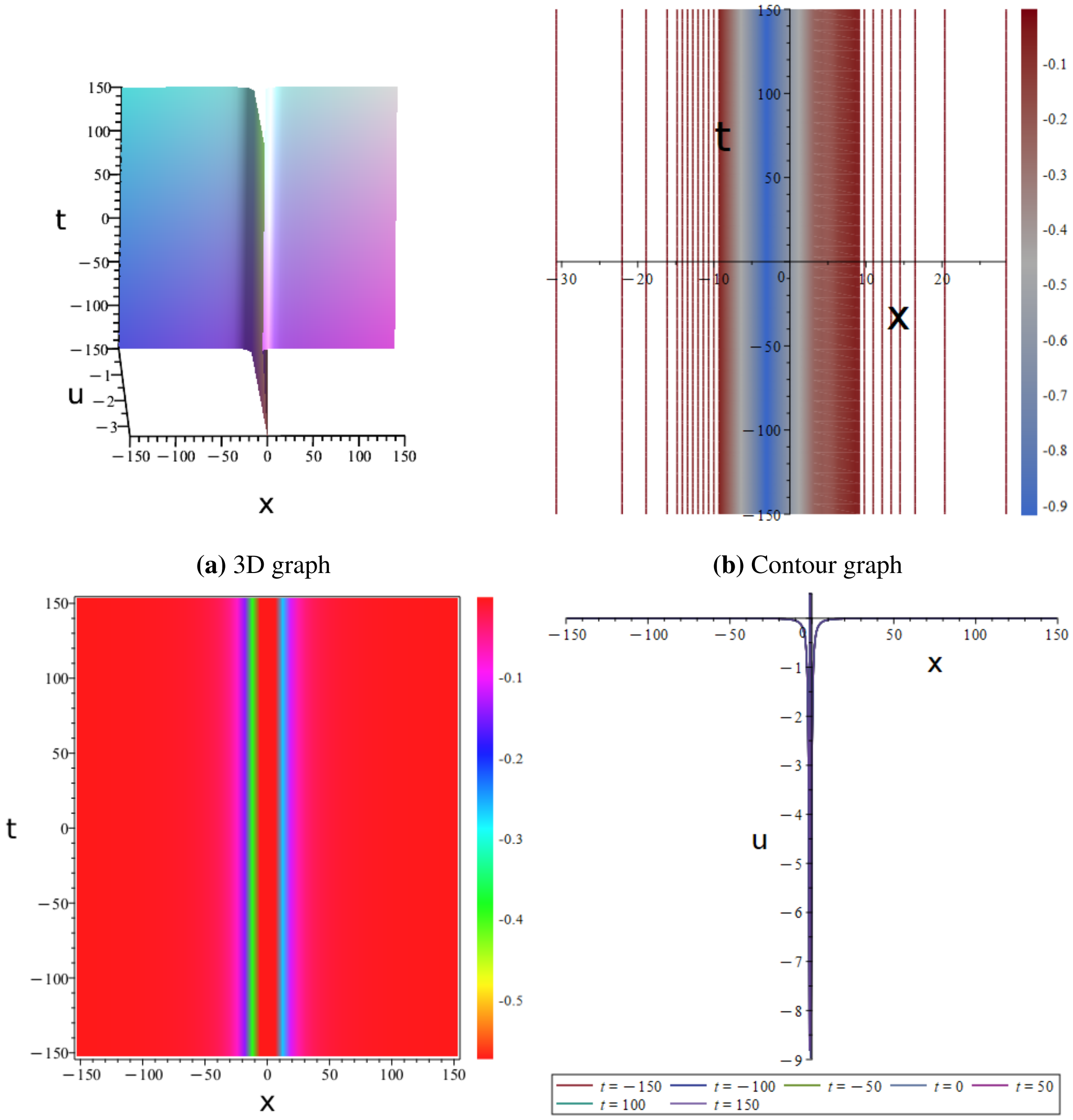

(a) 3D graph **(b)** Contour graph

(c) Density graph **(d)** Curve graph

Figure 9. 3D graph, contour graph, density graph, and curve graph of the solution to Eq (3.12).

3.2.2. Model 2-5-2-2-1 Case 2

The mathematical expression corresponding to the double-hidden-layer feature-enhanced 2-5-2-2-1 neural network model in Figure 10 was selected as the test function.

$$\begin{aligned}
\xi_1 &= w_{x,1} \cdot x + w_{t,1} \cdot t + w_{xt,1} \cdot xt + w_{x^2,1} \cdot x^2 + w_{t^2,1} \cdot t^2 + b_1, \\
\xi_2 &= w_{x,2} \cdot x + w_{t,2} \cdot t + w_{xt,2} \cdot xt + w_{x^2,2} \cdot x^2 + w_{t^2,2} \cdot t^2 + b_2, \\
\xi_3 &= w_{1,3} \cdot \xi_1 + w_{2,3} \cdot \xi_2 + b_3, \\
\xi_4 &= w_{1,3} \cdot \xi_1 + w_{2,3} \cdot \xi_2 + b_4, \\
f &= w_{3,f} \cdot \xi_3^2 + w_{4,f} \cdot \operatorname{sech}(\xi_4) + b_5.
\end{aligned} \tag{3.13}$$

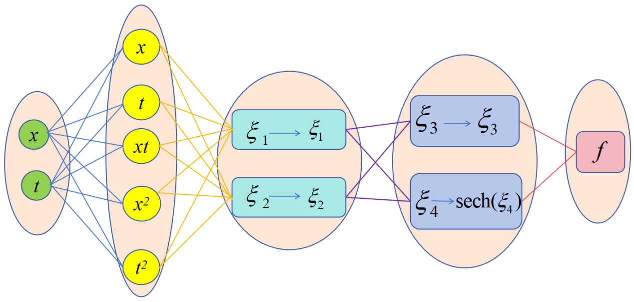

Figure 10. 2-5-2-2-1 neural network model with given activation functions $\Phi_1(\xi_1) = \xi_1$, $\Phi_2(\xi_2) = \xi_2$, $\Phi_3(\xi_3) = \xi_3^2$, $\Phi_4(\xi_4) = \mathrm{sech}(\xi_4)$.

As shown in Figure 10, the activation function $\Phi_1(\xi_1) = \xi_1$, $\Phi_2(\xi_2) = \xi_2$, $\Phi_3(\xi_3) = \xi_3^2$, $\Phi_4(\xi_4) = \mathrm{sech}(\xi_4)$ were set. Thus, the test functions for the solution were obtained as follows:

$$\begin{aligned} f =\ & b_5 + w_{3,f}\Big(w_{1,3}\left(t^2 w_{t^2,1} + txw_{xt,1} + x^2 w_{x^2,1} + tw_{t,1} + xw_{x,1} + b_1\right) \\ & + w_{2,3}\left(t^2 w_{t^2,2} + txw_{xt,2} + x^2 w_{x^2,2} + tw_{t,2} + xw_{x,2} + b_2\right) + b_3\Big) \\ & + w_{4,f}\mathrm{sech}\Big(w_{1,3}\left(t^2 w_{t^2,1} + txw_{xt,1} + x^2 w_{x^2,1} + tw_{t,1} + xw_{x,1} + b_1\right) \\ & + w_{2,3}\left(t^2 w_{t^2,2} + txw_{xt,2} + x^2 w_{x^2,2} + tw_{t,2} + xw_{x,2} + b_2\right) + b_3\Big); \end{aligned} \tag{3.14}$$

among them, $b_i\ (i = 1, 2, 3)$, $w_{j,f}\ (j = 1, 2)$ and $w_{k,1}\ (k = x, t, xt, x^2, t^2)$ were real numbers.

The solution test function (3.14) was substituted into the bilinear Eq (2.2). A complex algebraic equation was obtained. The coefficients of each term were collected and set to 0. Then, the equation could be satisfied. At this point, a system of algebraic equations was obtained and solved, yielding the following results:

$$\begin{aligned} w_{x,1} &= -\frac{2xw_{1,3}w_{x^2,1} + 2xw_{2,3}w_{x^2,2} + w_{2,3}w_{x,2}}{w_{1,3}}, \\ w_{t,1} &= -\frac{w_{2,3}w_{t,2}}{w_{1,3}}, \quad w_{4,f} = 0. \end{aligned} \tag{3.15}$$

Substitute (3.15) into the test function (3.14). Then, through the bilinear transformation (2.1), the explicit solution of the (1+1)-dimensional CDG Eq (1.1) was obtained as follows:

$$\begin{cases} u = \frac{2Ew_{3,f}}{(Cw_{1,3}+Dw_{2,3}+b_3)w_{3,f}+b_5} - \frac{2F^2 w_{3,f}^2}{\left((Cw_{1,3}+Dw_{2,3}+b_3)w_{3,f}+b_5\right)^2}, \\ C = t^2 w_{t^2,1} - x^2 w_{x^2,1} + tw_{t,1} + b_1, \\ D = t^2 w_{t^2,2} - x^2 w_{x^2,2} + tw_{t,2} + b_2, \\ E = -2w_{1,3}w_{x^2,1} - 2w_{2,3}w_{x^2,2}, \\ F = -2xw_{1,3}w_{x^2,1} - 2xw_{2,3}w_{x^2,2}. \end{cases} \tag{3.16}$$

To validate the accuracy of Result (3.16), the analytical solution (3.16) was substituted into the LHS of Eq (1.1). With the assistance of Maple software, the simplified result demonstrated that the LHS of Eq (1.1) equaled zero. This confirms that the analytical solution (3.16) is reliable, accurate, and error-free. It also highlights the advantage of this method: In contrast to classical neural network methods, which only yield approximate solutions, the bilinear feature-enhanced symbolic computation neural network algorithm enables the acquisition of exact analytical solutions. In solution (3.16), $w_{3,f} = 1, b_3 = 1, b_1 = 1, b_2 = 1$, and $w_{4,f} = 1, w_{t,3} = 1, w_{x,3} = 1, b_5 = 1, w_{t,1} = 2, w_{t,2} = 1, w_{x,1} = 1, w_{x,2} = 1, w_{t^2,1} = 1, w_{t^2,2} = 1$ were set. The graph of the solution could then be plotted (Figure 11).

Figure 11(a) displays the 3D graph when $t \in (-150, 150)$ and $x \in (-150, 150)$. It features a double "ridge-like" structure, presenting an intersecting hyperboloid morphology. The color gradient (blue-purple-red transition) corresponds to the amplitude distribution of u. The "ridge lines" of the surface are high-value regions, and the two sides are low-value regions. The "asymmetric inclination" and "intersecting distortion" of the surface embody the nonlinear interaction of the (1+1)-dimensional CDG equation, and the amplitude of the wave is nonuniformly distributed in spatiotemporal domains.

Figure 11(b) is the contour graph of solution (3.16). The contour lines are arranged in an "X"-shaped intersection, consistent with the hyperboloid intersecting morphology of the 3D graph, indicating that two waves propagate in opposite directions along the x and t axes. The dense contour lines and deep color (red-brown) in the intersection region correspond to the high-value regions of the wave, embodying the energy concentration characteristic of wave interaction. Energy superposition occurs when the two waves collide, forming a high-amplitude region.

Figure 11(c) is a density graph. A continuous color gradient (color bar on the right) is used to show the distribution of u in the x-t plane, where purple represents low-value regions (sparse energy), and colored intersecting stripes represent high-value regions with concentrated energy. The "X"-shaped colored stripes (yellow-red transition) extend along the x and t axes, corresponding to the hyperboloid "ridge lines" in the 3D graph, intuitively presenting the propagation trajectories and interaction regions of the two waves.

Figure 11(d) is a curve graph of u versus x in the domain $(-150, 150)$. The horizontal axis is x, the vertical axis is u, and multiple colored curves correspond to the distribution of $u(x)$ at different times t. Each curve exhibits a periodic multipeak morphology. The number and spacing of peaks correspond to the multiwave interference characteristic of the (1+1)-dimensional CDG equation solution. The peak height reflects the wave amplitude, the peak width reflects the spatial scale of the wave, and the peak spacing reflects the interaction period of the waves.

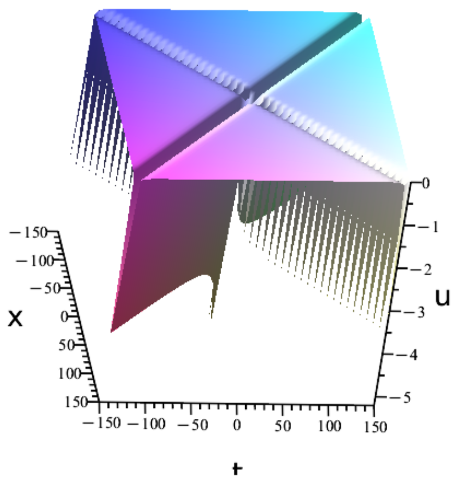

(a) 3D graph

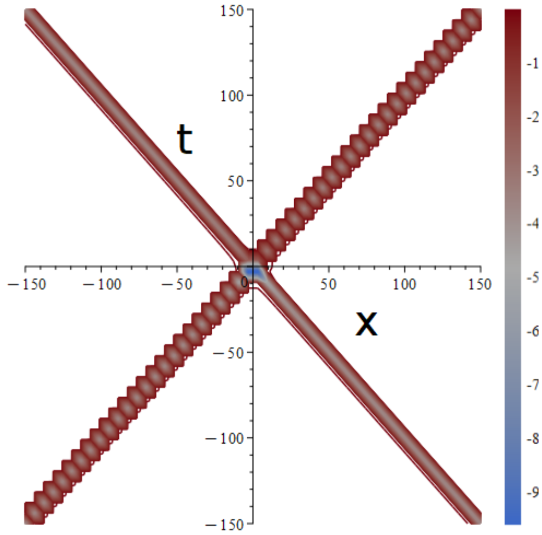

(b) Contour graph

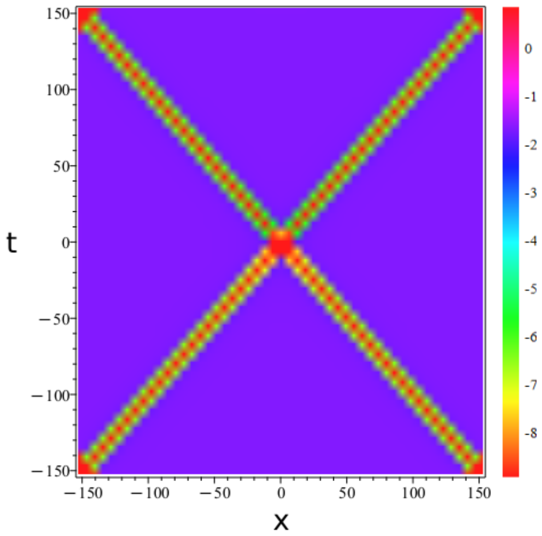

(c) Density graph

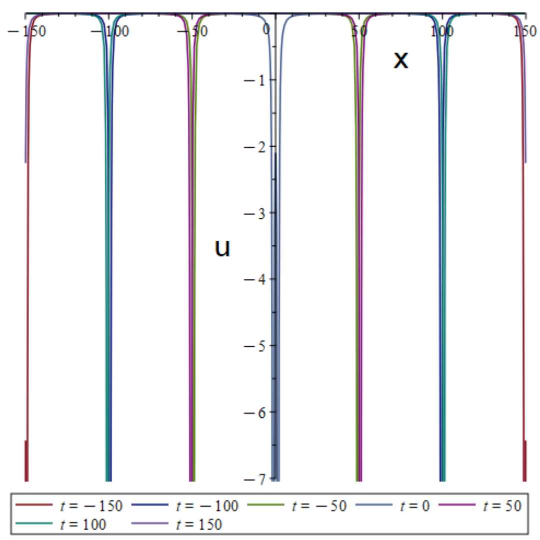

(d) Curve graph

Figure 11. 3D graph, contour graph, density graph, and curve graph of the solution to Eq (3.16).

3.3. Remark

This study proposes a BFESCNN method. By constructing single-hidden-layer 2-5-2-1 and double-hidden-layer 2-5-2-2-1 models, exact solutions to the (1+1)-dimensional CDG equation are obtained. Compared with existing research on solving the (1+1)-dimensional CDG equation, this method demonstrates significant innovation and advantages, with detailed comparative analysis provided in Tables 3 and 4.

Table 3. BFESCNN and various CDG equation solution methods comparison.

Comparison dimension	**BFESCNN (this study)**	**Traditional analytical methods (Hirota [13], etc.)**	**PINNs [23], etc.**	**BNNM [4], etc.**
Solution type and accuracy	Exact solutions (Maple-verified zero error); supports soliton-like, multiwave interference solutions	Analytical solutions (reliable accuracy); only breather, soliton, periodic trigonometric/hyperbolic solutions; one derivation for single solution type	Approximate numerical solutions; poor fractional derivative accuracy; invalid for stochastic Wick-type PDEs	Analytical solutions (reliable accuracy); generalized/classical lump and rogue waves achievable; hard to generate hybrid wave interaction solutions
Core logic	Polynomial feature enhancement and symbolic constraints and neural network (NN); no preset structure	Manual ansatz construction and algebraic/symbolic derivation; heavy human intervention; poor adaptability to fractional/variable-coefficient CDGSK equations	PDE residual embedded loss function; pure data-driven meshless solving; relies on high-quality stochastic/fractional dataset	Bilinear operator network and symbolic computation; experience-dependent design; only applicable to bilinear-form CDG/CDGSK-like equations
Network complexity	Concise single/double-hidden-layer architecture; "feature enhancement" instead of "neuron stacking"; high efficiency	No network; pure mathematical derivation; extremely high labor cost for seventh-order CDG-KP equation reduction	Deep network with massive trainable parameters; long training time and easy overfitting for fractional PDEs	Multilayer stacking hybrid model; high parameter optimization difficulty; slow convergence for multitype wave coupling
Interpre-tability	Clear physical feature meaning; traceable symbolic computation; visualizable wave propagation properties	Transparent mathematical derivation; extra physical interpretation required for fractional derivative wave characteristics	"Black-box" data learning; only infers physical meaning from numerical results; no mechanism interpretability	Bilinear physical constraints; unclear featurewave solution connection; needs post-analysis for lump wave evolution
Applicable scenarios	High-dimensional/variable-coefficient/strongly nonlinear PDEs; needs multitype exact solutions (e.g., plasma magnetoacoustic waves)	Low-dimensional/constant-coefficient CDG equations; specific traveling wave/periodic wave solutions with low efficiency demand	Meshless/data-scarce scenarios; low accuracy demand for fast approximate fractional PDE distribution	Medium-low dimensional CDGSK-like equations; tolerates high model complexity for lump/rogue wave generation
Computational efficiency	High (automated symbolic computation, fast training, no massive data)	Low (time-consuming manual symmetry reduction/derivation, no batch solving for series CDG family equations)	Medium (long training iteration, tedious parameter tuning for fractional order setting and data preprocessing)	Low (long training cycle, massive manual debugging for bilinear NN connection and wave solution coupling)

Table 4. BFESCNN and various CDG equation solution methods comparison (continued).

Comparison dimension	BFESCNN (this study)	Traditional analytical methods (Hirota [13], etc.)	PINNs [23], etc.	BNNM [4], etc.
Solution precision and stability	Ultra-high precision (zero numerical error); ultra-stable waveform output without distortion for fractional/high-order derivation	High precision for specific cases; stable results but limited to nonstochastic PDEs, no stability for seventh-order CDG-KP equations	Low precision with cumulative error; unstable waveform in long-term fractional wave evolution and stochastic PDE solving	Reliable precision; partial stability loss in lump-periodic wave coupling; sensitive to network hyperparameters
Analytical universality	Excellent; unified framework for CDG family equations; compatible with fractional/stochastic/(2+1)-dimensional/variable-coefficient PDEs	Poor universality; method-specific for different solution types; inapplicable to stochastic Wick-type fractional PDEs	Medium universality; meshless advantage but limited by training data for unseen CDG equation forms	Limited universality; structure-bound to bilinear PDE systems, hard to transfer to nonbilinear CDG-KP equations

4. Conclusions

The BFESCNN method adopts an integrated approach of "polynomial feature enhancement, symbolic computation, and neural network". It breaks through the limitations of traditional methods for solving the (1+1)-dimensional CDG equation. The method efficiently acquires the exact solution of the equation. Multidimensional graphs (3D graphs, density plots, contour plots, curve graphs) are used to verify the rationality of the solution and the advantages of the algorithm. It also provides visualization support for practical physical problems. Based on the spatial and temporal variables of the (1+1)-dimensional CDG equation, polynomial features x^2, t^2, and xt are constructed. These features accurately capture the nonlinear interaction relationships between variables. They make up for the deficiency of traditional neural networks that rely solely on original variables. The bilinear features provide a flexible and generalizable representation of nonlinear interactions, making it straightforward to extend to more complex scenarios. Collectively, these solutions illustrate diverse nonlinear dynamical behaviors. Solution (3.4) demonstrates the interaction among multiple fundamental excitations, verifying the robustness of solitons as information carriers and providing insights for engineering applications such as optical soliton communication, and Solution (3.8) focuses on the adaptation and evolution of a single coherent structure under complex physical conditions, aiding in the design of novel nonlinear wave manipulation schemes. Solution (3.12) represents a static ordered structure arising from self-organization, serving as a paradigm for energy localization, and Solution (3.16) depicts a dynamically coherent structure exhibiting controlled motion, which forms the cornerstone for wavepacket manipulation. Furthermore, the method offers quantifiable and visual analytical basis for practical physical problems. Such problems include plasma ion-acoustic waves and optical fiber light pulses. It serves as an important bridge connecting nonlinear equation theory and interdisciplinary applications.

Building upon the bilinear feature-enhanced symbolic computation neural network algorithm for exact solutions of nonlinear PDEs, the methodology in [41] can refine random-term handling, an [42, 43] can augment the algorithm's stability and robustness. Moreover, integrating insights from [44, 45] can further optimize the algorithm's neural network framework. This algorithm may be extended to multisource random perturbation systems, with the "solution-verification-simplification" framework refined to boost cross-domain applicability, thus fostering interdisciplinary innovation in exact solutions of stochastic nonlinear PDEs.

Author contributions

Xia Li: Conceptualization, methodology, validation, writing–original draft preparation, writing–review and editing, supervision, project administration, funding acquisition; Jianglong Shen: Conceptualization, methodology, validation, writing–review and editing, supervision, project administration, funding acquisition; Jingbin Liang: writing–original draft preparation, validation; Yu Gao: writing–original draft preparation, validation, project administration, supervision, funding acquisition. All authors have read and approved the final version of the manuscript for publication.

Use of Generative-AI tools declaration

The authors declare they have not used Artificial Intelligence (AI) tools in the creation of this article.

Acknowledgments

This work was supported by Training Program of Yibin University (No.2022PY29), Training Program of Yibin University (No.2024XJPY13), Sailing Project of Yibin University (No.2024XJQH04), and the Open Research Fund of Computational Physics Key Laboratory of Sichuan Province, Yibin University (No.YBUJSWL-KX-2025-04).

Conflict of interest

The authors declare that they have no conflict of interest concerning the publication of this manuscript.

References

1. E. Hussain, A. H. Tedjani, K. Farooq, Beenish, Modeling and exploration of localized wave phenomena in optical fibers using the generalized Kundu–Eckhaus equation for femtosecond pulse transmission, *Axioms*, **14** (2025), 513. https://doi.org/10.3390/axioms14070513
2. M. A. S. Murad, F. S. Alshammari, M. S. Salih, K. Farooq, Optical soliton structures in the nonlinear conformable Schrödinger equation with quadratic–cubic nonlinearity, *Nonlinear Dynam.*, **113** (2025), 32669–32687. https://doi.org/10.1007/s11071-025-11775-z
3. K. Farooq, A. H. Tedjani, Z. Li, E. Hussain, Soliton dynamics of the nonlinear Kodama equation with M-truncated derivative via two innovative schemes: The generalized Arnous method and the Kudryashov method, *Fractal Fract.*, **9** (2025), 436. https://doi.org/10.3390/fractalfract9070436

4. R. F. Zhang, M. C. Li, M. Albishari, F. C. Zheng, Z. Z. Lan, Generalized lump solutions, classical lump solutions and rogue waves of the (2+1)-dimensional Caudrey-Dodd-Gibbon-Kotera-Sawada-like equation, *Appl. Math. Comput.*, **403** (2021), 126201. https://doi.org/10.1016/j.amc.2021.126201
5. L. Gai, W. Wu, T. Ding, Y. Qian, Lump wave solutions, lump-stripe soliton inelastic collision phenomena and rogue-type wave solutions for a generalized breaking soliton system in (3+1)-dimensions, *Wave Motion*, **124** (2024) , 103243. https://doi.org/10.1016/j.wavemoti.2023.103243
6. Z. H. Zhang, J. G. Liu, A fourth-order nonlinear equation studied by using a multivariate bilinear neural network method, *Nonlinear Dynam.*, **112** (2024), 10229–10237. https://doi.org/10.1007/s11071-024-09567-y
7. X. S. Wu, J. G. Liu, Solving the variable coefficient nonlinear partial differential equations based on the bilinear residual network method, *Nonlinear Dynam.*, **112** (2024), 8329–8340. https://doi.org/10.1007/s11071-024-09472-4
8. X. Hao, Y. Liu, X. Tang, Z. Li, A Maple package for finding interaction solutions of nonlinear evolution equations, *Comput. Math. Appl.*, **72** (2016), 2450–2461. https://doi.org/10.1016/j.camwa.2016.09.006
9. R. Hirota, *The direct method in soliton theory*, Cambridge University Press, 2004. https://doi.org/10.1017/CBO9780511543043
10. V. Kumar, A. K. Pandey, D. S. Bisht, Multisoliton solutions and interaction of solitons for the (3+1)-dimensional Calogero-Degasperis-Gibbon equation, *Chinese Phys. B*, **31** (2022), 100203 https://doi.org/10.1088/1674-1056/ac8cbe
11. J. Singh, A. Gupta, D. Baleanu, On the analysis of an analytical approach for fractional Caudrey-Dodd-Gibbon equations, *Alex. Eng. J.*, **61** (2022), 5073–5082. https://doi.org/10.1016/j.aej.2021.09.053
12. G. F. Deng, Y. T. Gao, J. J. Su, C. C. Ding, T. T. Jia, Solitons and periodic waves for the (2+1)-dimensional generalized Caudrey–Dodd–Gibbon–Kotera–Sawada equation in fluid mechanics, *Nonlinear Dynam.*, **99** (2020), 1039–1052. https://doi.org/10.1007/s11071-019-05328-4
13. A. Yusuf, T. A. Sulaiman, M. Inc, M. Bayram, Breather wave, lump-periodic solutions and some other interaction phenomena to the Caudrey–Dodd–Gibbon equation, *Eur. Phys. J. Plus*, **563** (2020), 135. https://doi.org/10.1140/epjp/s13360-020-00566-7
14. M. M. A. Khater, S. H. Alfalqi, Analytical solutions of the Caudrey–Dodd–Gibbon equation using Khater II and variational iteration methods, *Sci. Rep.*, **14** (2024), 27946. https://doi.org/10.1038/s41598-024-75969-y
15. A. Yokuş, H. Durur, K. A. Abro, Symbolic computation of Caudrey–Dodd–Gibbon equation subject to periodic trigonometric and hyperbolic symmetries, *Eur. Phys. J. Plus*, **358** (2021), 136. https://doi.org/10.1140/epjp/s13360-021-01350-x
16. A. K. M. K. S. Hossain, M. A. Akbar, M. I. Hossain, Modified simple equation technique for first-extended fifth-order nonlinear equation, medium equal width equation and Caudrey–Dodd–Gibbon equation, *J. Umm Al-Qura Univ. Appl. Sci.*, **11** (2025), 623–632.
17. H. Ma, Y. Wang, A. Deng, Soliton molecules and some novel mixed solutions for the extended Caudrey-Dodd-Gibbon equation, *J. Geom. Phys.*, **168** (2021), 104309. https://doi.org/10.1016/j.geomphys.2021.104309

18. A. F. Şahinkaya, A. Kurt, İ. Yalçınkaya, Investigating the new perspectives of Caudrey–Dodd–Gibbon equation arising in quantum field theory, *Opt. Quant. Electron.*, **56** (2024), 813. https://doi.org/10.1007/s11082-024-06636-9
19. S. A. Abdelhafeez, A. A. M. Arafa, Y. H. Zahran, I. S. I. Osman, M. Ramadan, Adapting Laplace residual power series approach to the Caudrey Dodd Gibbon equation, *Sci. Rep.*, **14** (2024), 9772. https://doi.org/10.1038/s41598-024-57780-x
20. D. Fathima, R. A. Alahmadi, A. Khan, A. Akhter, A. H. Ganie, An efficient analytical approach to investigate fractional Caudrey–Dodd–Gibbon equations with non-singular Kernel derivatives, *Symmetry*, **15** (2023), 850. https://doi.org/10.3390/sym15040850
21. Q. Ding, A. J. Hao, Differential invariants for CDG equation and coupled KDV-MKDV equations, *Acta Phys. Sin.*, **63** (2014), 110503. https://doi.org/10.7498/aps.63.110503
22. S. Sakovich, A note on lax pairs of the Sawada-Kotera equation, *J. Math.*, **4** (2014), 906165. https://doi.org/10.1155/2014/906165
23. M. Raissi, G. E. Karniadakis, Hidden fluid mechanics: Learning velocity and pressure fields from flow visualization, *Science*, **367** (2020), 1026–1030. https://doi.org/10.1126/science.aaw4741
24. S. Wang, B. Li, Y. Chen, P. Perdikaris, Piratenets: Physics-informed deep learning with residual adaptive networks, *J. Mach. Learn. Res.*, **25** (2024), 1–51. http://jmlr.org/papers/v25/24-0313.html
25. J. L. Shen, R. F. Zhang, J. W. Huang, J. B. Liang, Neural network-based symbolic computation algorithm for solving (2+1)-dimensional Yu-Toda-Sasa-Fukuyama equation, *Mathematics*, **13** (2025), 3006. https://doi.org/10.3390/math13183006
26. M. Raissi, P. Perdikaris, G. E. Karniadakis, Physics-informed neural networks: A deep learning framework for solving forward and inverse problems involving nonlinear partial differential equations, *J. Comput. Phys.*, **378** (2019), 686–707. https://doi.org/10.1016/j.jcp.2018.10.045
27. L. Lu, X. Meng, Z. Mao, G. E. Karniadakis, DeepXDE: A deep learning library for solving differential equations, *SIAM Rev.*, **63** (2021), 208–228. https://doi.org/10.1137/19M1274067
28. G. E. Karniadakis, I. G. Kevrekidis, L. Lu, P. Perdikaris, S. F. Wang, L. Yang, Physics-informed machine learning, *Nat. Rev. Phys.*, **3** (2021), 422–440. https://doi.org/10.1038/s42254-021-00314-5
29. W. Hussain, J. M. Merigó, J. Gil-Lafuente, H. H. Gao, Complex nonlinear neural network prediction with IOWA layer, *Soft Comput.*, **27** (2023) ,4853–4863. https://doi.org/10.1007/s00500-023-07899-2
30. X. Q. Huang, W. L. Shi, X. T. Gao, X. R. Wei, J. Zhang , J. Bian, et al., LordNet: An efficient neural network for learning to solve parametric partial differential equations without simulated data, *Neural Networks*, **176** (2024), 106354. https://doi.org/10.1016/j.neunet.2024.106354
31. S. Chen, S. Xiong, Y. Liu, Chebyshev-Sobolev physics-informed neural networks for general PDE solutions, *Int. J. Appl. Comput. Math.*, **11** (2025), 169. https://doi.org/10.1007/s40819-025-01988-6
32. J. L. Shen, X. Y. Wu, Periodic-soliton and periodic-type solutions of the (3+1)-dimensional Boiti–Leon–Manna–Pempinelli equation by using BNNM, *Nonlinear Dynam.*, **106** (2021), 831–840. https://doi.org/10.1007/s11071-021-06848-8

33. M. Qasim, F. Yao, M. Z. Baber, U. Younas, Investigating the higher dimensional Kadomtsev–Petviashvili–Sawada–Kotera–Ramaniequation: Exploring the modulation instability, Jacobi elliptic and soliton solutions, *Phys. Scripta*, **100** (2025), 025215. https://doi.org/10.1088/1402-4896/ada20c
34. L. Ying, M. Li, Y. Shi, New exact solutions and related dynamic behaviors of a (3+1)-dimensional generalized Kadomtsev–Petviashvili equation, *Nonlinear Dynam.*, **112** (2024), 11349–11372. https://doi.org/10.1007/s11071-024-09539-2
35. Z. Liu, Y. Liu, X. Yan, W. Liu, H. Nie, S. Guo, et al., Automatic network structure discovery of physics informed neural networks via knowledge distillation, *Nat. Commun.*, **16** (2025), 9558. https://doi.org/10.1038/s41467-025-64624-3
36. S. F. Sun, S. F. Tian, B. Li, The data-driven rogue waves of the Hirota equation by using Mix-training PINNs approach, *Physica D*, **465** (2024), 134202. https://doi.org/10.1016/j.physd.2024.134202
37. J. L. Shen, M. Liu, J. B. Liang, R. F. Zhang, New solutions to the (3+1)-dimensional HB equation using bilinear neural networks method and symbolic ansatz method using neural network architecture, *AIMS Math.*, **10** (2025), 30307–30330. https://doi.org/10.3934/math.20251331
38. P. J. Caudrey, R. K. Dodd, J. D. Gibbon, A new hierarchy of Korteweg–de Vries equations, *Proc. A.*, **351** (1976), 407–422. https://doi.org/10.1098/rspa.1976.0149
39. H. Naher, F. A. Abdullah, M. A. Akbar, The (G'/G)-expansion method for abundant traveling wave solutions of Caudrey-Dodd-Gibbon equation, *Math. Probl. Eng.*, **2011** (2011), 218216. https://doi.org/10.1155/2011/218216
40. K. Ayub, M. Y. Khan, A. Rani, Q. M. Ul Hassan, B. Ahmed, M. Shakeel, Application of the Exp $(-\phi(\zeta))$-expansion method for solitary wave solutions., *Arab J. Basic Appl. Sci.*, **26** (2019), 376–384. https://doi.org/10.1080/25765299.2019.1642079
41. K. E. Yao, M. Samar, Y. Shi, Approximation approach for backward stochastic Volterra integral equations, *Math. Model. Control*, **4** (2024), 390–399. https://doi.org/10.3934/mmc.2024031
42. Y. Lu, D. Ruan, Q. Zhu, Stability of nonlinear systems with multi-delayed random impulses: Average estimation and delay approach, *Nature*, **1** (2025), 2. https://doi.org/10.3934/math.2025982
43. J. Y. Yan, B. Hu, Z. H. Guan, D. X. Zhang, On controllability of fractional-order impulsive and switching systems with time delay, *Appl. Math. Comput.*, **497** (2025), 129357. https://doi.org/10.1016/j.amc.2025.129357
44. C. Lv, X. L. Lv, Z. Y. Wang, A focal quotient gradient system method for deep neural network training, *Appl. Soft Comput.*, **184** (2025), 113704. https://doi.org/10.1016/j.asoc.2025.113704
45. M. Y. Gao, S. Y. Zhou, W. Gu, MMGPT4LF: Leveraging an optimized pre-trained GPT-2 model with multi-modal cross-attention for load forecasting, *Appl. Energy*, **392** (2025), 125965. https://doi.org/10.1016/j.apenergy.2025.125965

AIMS Press